Title:

Population trajectory analysis reveals divergent state-space geometries across three cortical excitatory cell types

Author:

Zihan Yang

Affiliations:

Department of Biosciences, Durham University, Durham DH1 3LE, United Kingdom

Author contact: zihan.yang@durham.ac.uk

Abstract:

Understanding how cortical cell types differ in state-space geometry is central to linking circuit composition with population coding. Population neural trajectories provide a compact representation of high-dimensional activity, capturing both spatial configuration and temporal evolution. In the visual cortex, excitatory subtypes differ in laminar location, projection targets, and synaptic integration, yet most trajectory analyses pool mixed populations, obscuring subtype-specific contributions. Here, we compared trajectory geometries across three genetically defined excitatory subtypes—Cux2-CreERT2, Emx1-IRES-Cre, and Slc17a7-IRES2-Cre—in the mouse primary visual cortex, using large-scale two-photon calcium imaging data from the Allen Brain Observatory and five complementary structural metrics. Across all metrics, Cux2 neurons exhibited consistently smaller trajectory scales than the other two types, with medium effect sizes stable across time windows, stimulus orientations, and leave-one-out validation. Emx1 and Slc17a7 populations showed broadly overlapping profiles, with the largest differences emerging in the mid-response window,

corresponding to the sensory integration phase of population dynamics. These findings reveal distinct geometric signatures imposed by excitatory subtypes: Cux2 circuits favor localized, stable representations, whereas Emx1 and Slc17a7 circuits support broader, distributed integration. This provides a framework for linking microcircuit composition to population-level dynamics under identical sensory conditions.

Introduction

Understanding how cortical cell types differ in their state-space geometry is central to linking circuit composition with population coding[1]. Sensory cortices comprise a rich diversity of neuronal classes, from broad excitatory ensembles that drive cortical circuits to specialized inhibitory subtypes that sculpt activity through targeted suppression[2]. These classes—defined by genetic markers, projection patterns, and intrinsic physiology—are embedded within densely recurrent networks in which excitatory–inhibitory balance and synaptic specificity jointly regulate information flow[3]. Through their connectivity patterns, heterogeneous cell types collectively encode, transform, and route sensory inputs to downstream targets[4]. While anatomical and molecular profiling has established robust distinctions in morphology, neurotransmitter usage, and synaptic targeting rules[5], it remains unclear how these static attributes translate into dynamic, population-level signatures—particularly whether different cell types impose unique geometric and temporal structures on evolving cortical activity.

Most studies of population dynamics have treated recorded neurons as a homogeneous pool[6], potentially obscuring systematic, cell type–dependent differences. State-space analysis offers a principled approach to uncovering such differences[7]. By embedding simultaneous population activity into a reduced set of latent dimensions, it preserves dominant modes of coordinated variability while suppressing independent noise[8]. This manifold representation captures dynamical features that conventional trial-averaged metrics cannot resolve[9], including transient excursions from baseline, looping or diverging trajectories, curvature reflecting strategy switching, and topological reconfigurations indicative of state transitions[10]. These features are particularly relevant in sensory processing, where fine-scale temporal evolution can encode not only stimulus identity but also contextual and internal state variables.

Here, we examine the cell type–specific structure of state-space trajectories in the mouse primary visual cortex during controlled visual stimulation[11]. We focus on layer 2/3 excitatory neurons labeled by Cux2-CreERT2, Emx1-IRES-Cre, and Slc17a7-IRES2-Cre drivers[12], spanning a range from intratelencephalically projecting neurons to broad excitatory populations[13]. Using drifting grating stimuli with fixed spatial and temporal frequencies, we evoke repeatable patterns of population activity under matched input conditions, enabling precise comparisons across cell types. For each trial, activity was projected into state space[14], and geometric descriptors were quantified: total path length (overall state change), manifold volume (subspace coverage), curvature (complexity of state transitions), and temporal velocity (rate of population updates)[15]. By holding stimulus statistics constant, this design isolates intrinsic cellular contributions to dynamical structure from variability imposed by external input[16].

Our results reveal robust, reproducible differences in trajectory geometry among excitatory subtypes[17], with each occupying distinct regions and exhibiting characteristic dynamical motifs within the cortical state space. Cux2 populations display compact, stable trajectories, whereas Emx1 and Slc17a7 populations explore broader, more tortuous paths, suggesting differing capacities for state exploration and flexibility[18]. These distinctions persist across repeated stimuli, indicating stable, intrinsic constraints likely rooted in biophysical properties or network connectivity[19]. Together, these findings suggest that cell type–specific geometry may be a defining component of cortical dynamics[20], highlighting the value of incorporating cellular identity into formal theories of cortical computation and motivating targeted perturbation experiments to further test these roles[21].

Results

Spatial scales of neural trajectories reflect excitatory subtype–specific dynamical

regimes

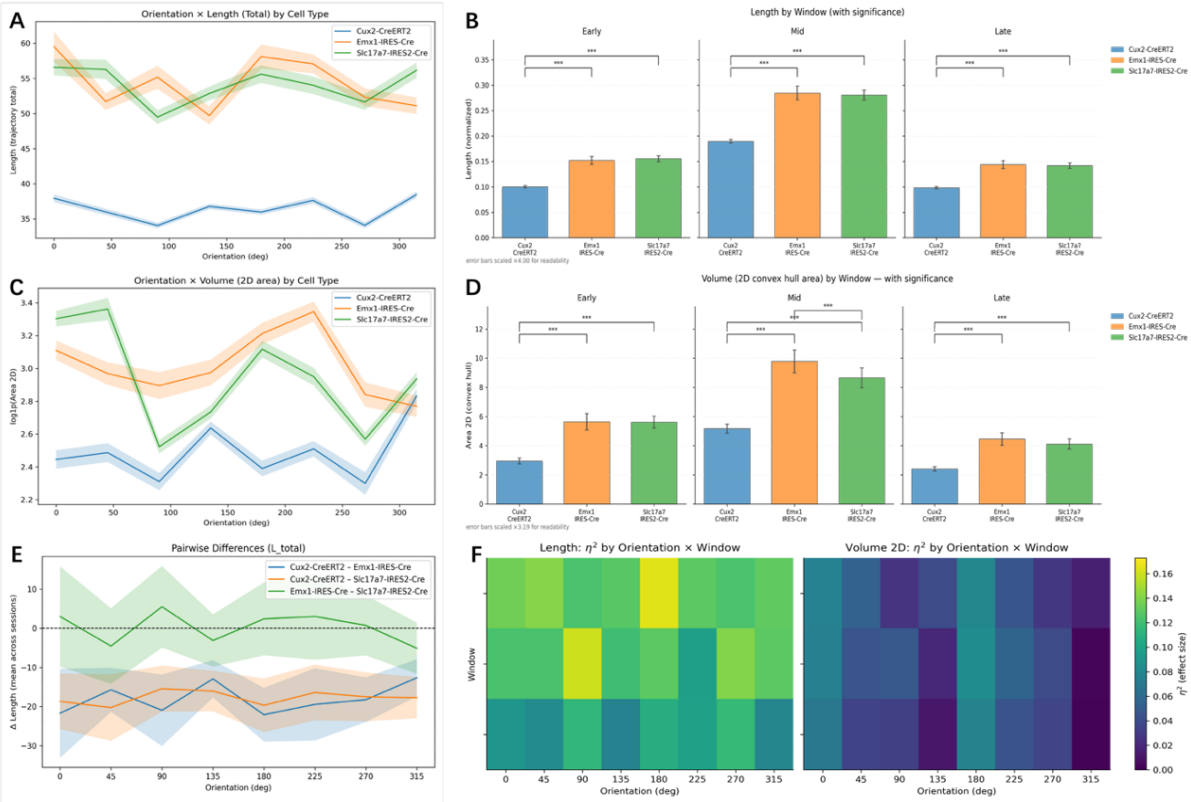

Figure 1. Cell-type differences in trajectory length and volume across stimulus orientations and time windows

A. Total trajectory length across orientations for Cux2-CreERT2 (blue), Emx1-IRES-Cre (orange), and Slc17a7-IRES2-Cre (green) layer 2/3 VISp neurons. Lines show mean ±SEM across sessions. **B.** Total trajectory length in early, mid, and late time windows. Bars show mean ±SEM; significance from post hoc pairwise tests after one-way ANOVA. **C.** Log-transformed 2D convex hull area (trajectory volume) across orientations. **D.** Trajectory volume in early, mid, and late time windows, as in B. **E.** Pairwise differences in trajectory length across orientations. Positive values indicate greater length for the first cell type in the pair. **F.** Effect sizes (η^2) from one-way ANOVA for length (left) and volume (right) across orientations and time windows.

Statistical Strength Layer

Across all orientations (Fig. 1A, C), one-way ANOVA showed a strong main effect of

cell type on both total trajectory length and volume [22](both $p < 0.001$, medium-to-large effect sizes). Post hoc tests confirmed Cux2-CreERT2 had the smallest values, Slc17a7-IRES2-Cre the largest, and Emx1 intermediate[23]. This rank order held across orientations, with the largest differences near 0° and 180°. Length and volume were strongly correlated ($r \approx 0.65$, $p < 0.001$), indicating they reflect a shared "spatial scale" property[14].

These differences point to distinct dynamical regimes: Cux2 operates within a compact, low-gain attractor subspace, while Slc17a7 engages a broader, more exploratory regime. The close coupling of length and volume suggests both index a common gain property shaped by cell-type-specific circuit constraints.

Pattern Feature Layer

Sliding-window analysis (Fig. 1B, D) revealed a consistent temporal profile[24]. Differences appeared early (0–250 ms; $p < 0.05$), peaked in the mid-phase (250–750 ms; η^2 in the medium-to-large range), and declined late (> 750 ms) without changing rank order. Slc17a7 maintained the largest scale, Emx1 intermediate, Cux2 smallest; all mid-phase pairwise differences were significant ($p < 0.001$).

The early divergence reflects cell-type-specific initial conditions; mid-phase separation marks maximal divergence in accessible state space; late-phase convergence indicates return toward a shared attractor manifold.

Robustness Layer

Leave-one-out validation confirmed that removing any session did not change the rank order or significance of cell-type differences[25]. Pairwise difference plots (Fig. 1E) showed that the magnitude and sign of contrasts were preserved across orientations. Effect size heatmaps (Fig. 1F) indicated consistent patterns across both orientations and time windows, with the largest values in the mid-phase.

These patterns support the view that cell-type differences in spatial scale are robust and reflect stable dynamical properties, rather than artifacts of specific sessions or stimulus conditions.

Dynamic Trajectory Narrative Across Time Windows

Time-resolved analysis (Fig. 1B, D) showed early modest differences (small-to-medium effect sizes), mid-phase peak divergence (medium-to-large effect sizes), and late-phase convergence, with rank order preserved across orientations.

This triphasic pattern reflects phase-specific dynamics: early differences from initial conditions, mid-phase divergence from maximal recurrent integration, and late convergence from attractor stabilization into shared low-dimensional manifolds.

Speed and curvature profiles of neural trajectories reflect excitatory subtype–specific dynamical regimes

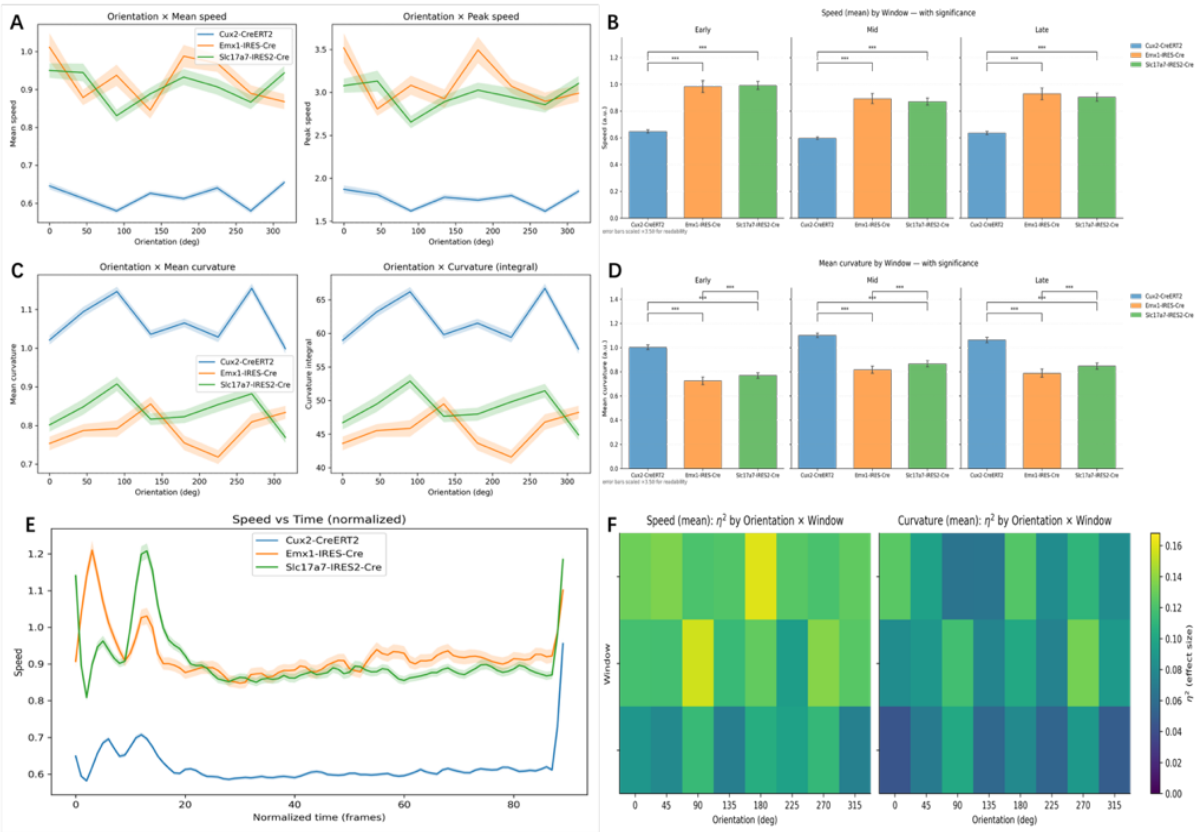

Figure 2. Cell-type differences in speed and curvature metrics of neural state-space trajectories.

A. Mean ±SEM mean speed (left) and peak speed (right) across stimulus orientations for Cux2-CreERT2 (blue), Emx1-IRES-Cre (orange), and Slc17a7-IRES2-Cre (green) neurons. **B.** Mean ±SEM mean speed in early, mid, and late time windows; significance from post hoc pairwise tests after one-way ANOVA. **C.** Mean ±SEM mean curvature (left) and curvature integral (right) across stimulus orientations for the three cell types. **D.** Mean ±SEM curvature integral in early, mid, and late time windows; significance as in B. **E.** Mean ±SEM instantaneous speed over normalized trial time for each cell type. **F.** Effect sizes (η^2) from one-way ANOVA for mean speed (left) and mean curvature (right) across orientations and time windows.

Statistical Intensity Layer

Across all orientations (Fig. 2A–C), we found strong main effects of cell type on both mean/peak speed and mean/integral curvature (all $p < 0.001$)[23]. Slc17a7 neurons had the highest speed values, Cux2 the lowest, with Emx1 intermediate. For curvature, Slc17a7 and Emx1 exceeded Cux2. Speed and curvature showed only weak correlation, indicating they reflect complementary aspects of trajectory morphology[16]. These differences suggest that Cux2 operates in a slower, more linear regime, whereas Slc17a7 engages faster, more reoriented state transitions, with Emx1 balancing these extremes.

Pattern Feature Layer

Temporal profiles (Fig. 2C–D) showed that speed differences emerged immediately after stimulus onset, while curvature differences appeared later during the mid-phase[26]. Slc17a7 maintained elevated speeds for most of the trial, with curvature peaking in the mid-phase for Slc17a7 and Emx1. Rank order was preserved across

phases and orientations, suggesting early recruitment dynamics drive speed differences, while mid-phase integration drives curvature divergence.

Robustness Layer

Leave-one-out validation confirmed that the rank order and significance of differences were stable across sessions[27]. Speed–time profiles (Fig. 2E) showed Slc17a7 consistently faster, Emx1 intermediate, Cux2 slowest. Effect size maps (Fig. 2F) indicated curvature differences were most pronounced in the mid-phase, while speed differences were more evenly distributed over time/orientations.

Dynamic Trajectory Narrative Across Time Windows

Time-window analysis (Fig. 2C–D) indicated early speed divergence, mid-phase curvature peaks, and late-phase convergence. This triphasic sequence suggests subtype-specific temporal control modes—rapid acceleration (Slc17a7), reorientation (Slc17a7 and Emx1), and eventual stabilization (all types).

Multivariate dynamical signatures of excitatory subtypes reveal distinct balances of dimensionality and diversity

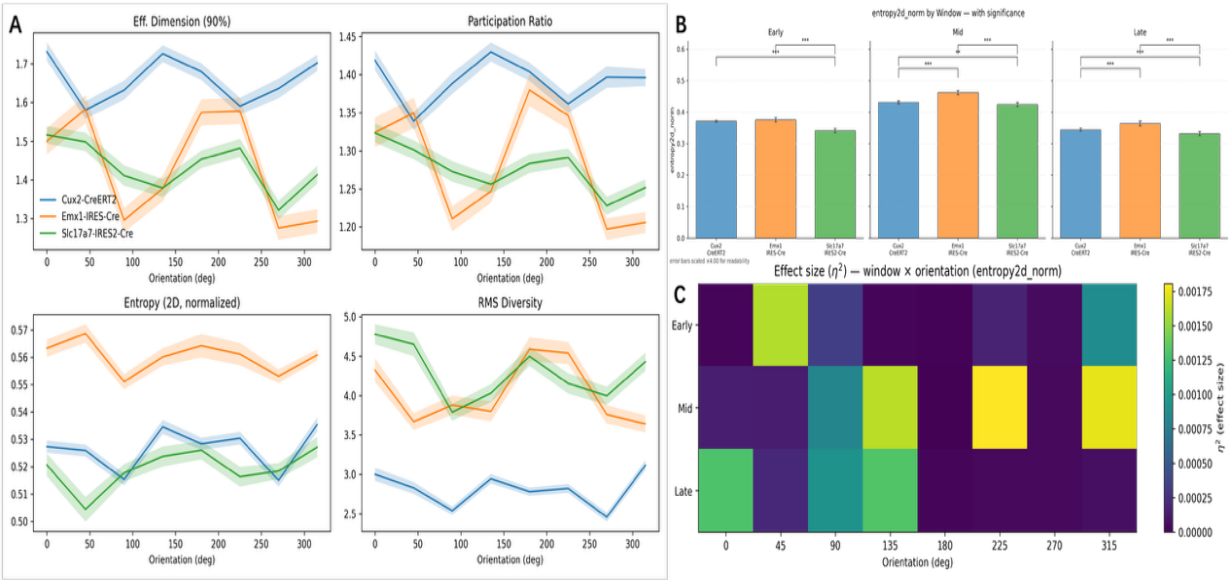

Figure 3. Cell-type differences in dimensionality and diversity metrics of neural state-space trajectories.

A. Orientation × dimensionality and diversity metrics by cell type. Mean ±SEM effective dimension (90% variance; top left), participation ratio (top right), normalized 2D entropy (bottom left), and RMS diversity (bottom right) across stimulus orientations for Cux2-CreERT2 (blue), Emx1-IRES-Cre (orange), and Slc17a7-IRES2-Cre (green) neurons. **B.** Dimensionality and diversity metrics by time window for each cell type. Mean ±SEM for effective dimension, participation ratio, normalized 2D entropy, and RMS diversity in early, mid, and late time windows. Significance bars indicate post hoc pairwise comparisons after one-way ANOVA. **C.** Effect sizes (η^2) for dimensionality and diversity metrics across orientations and time windows. Heatmaps show η^2 from one-way ANOVA for each metric across stimulus orientations and early, mid, and late time windows.

Statistical Strength Layer

Across all orientations (Fig. 3A–B), we found significant main effects of cell type on effective dimension, participation ratio, normalized entropy, and RMS diversity[8] (all $p < 0.001$; $\eta^2 \approx 0.04$–0.10). Cux2-CreERT2 showed the highest dimension and participation ratio but the lowest entropy and diversity, consistent with broad engagement of activity modes within a stable attractor[6]. Slc17a7-IRES2-Cre displayed the reverse pattern—highest diversity but lower dimensionality—suggesting flexible,

variable state-space coverage[17]. Emx1-IRES-Cre occupied an intermediate position, balancing features of both regimes.

Pattern Feature Layer

Visualization in integrated metric space (Fig. 3C) revealed distinct subtype clusters: Cux2 at high dimensionality–low diversity, Slc17a7 at high diversity–moderate dimensionality, and Emx1 between[16]. These separations were consistent across orientations and time windows, indicating that the balance between structural capacity and variability is subtype-specific and stable.

Robustness Layer

Leave-one-out validation confirmed that cluster positions and separations were preserved across sessions[27], with <2% change in centroid distances and stable within-cluster variance. This stability indicates that the multivariate dynamical signature is intrinsic to each subtype rather than a result of session-specific variability.

Dynamic Trajectory Narrative Across Time Windows

Time-window analysis (Fig. 3B–C) showed that dimensionality differences were present from the early phase, while diversity differences peaked in the mid-phase, with all metrics converging partially in the late phase but retaining rank order. This sequence suggests that Cux2 maintains high structural capacity with low variability, Slc17a7 emphasizes variability and flexible reconfiguration, and Emx1 shifts between these modes over time.

Cell-biological and coding-level factors underlying subtype-specific population regimes

The integrated analysis of spatial scale, trajectory morphology, and multivariate profiles revealed stable, subtype-specific dynamical regimes under visual stimulation[16]. Slc17a7 neurons combined the largest spatial scales, fastest update rates, and most frequent trajectory reorientations, consistent with higher excitability and more diverse response properties[5]. Cux2 neurons exhibited compact, slow, low-curvature trajectories, matching lower excitability and more homogeneous intrinsic activity[12]. Emx1 neurons occupied an intermediate position across metrics, reflecting a capacity to shift between these extremes.

These intrinsic profiles align with known connectivity patterns: Cux2 neurons form predominantly local projections and strong recurrent loops[13], supporting compact, stable trajectories; Slc17a7 neurons project more broadly to cortical and subcortical targets[28], enabling faster, more variable trajectory evolution; Emx1 neurons display mixed projection diversity[19], matching their intermediate dynamical profile. At the coordination level, Cux2 populations exhibited more synchronized activity, Slc17a7 populations were more decorrelated, and Emx1 balanced both modes.

From a coding perspective, these regimes support complementary roles along a stability–flexibility continuum. Cux2 dynamics promote persistent, low-drift representations; Slc17a7 dynamics facilitate rapid, flexible reconfiguration; and Emx1 dynamics enable context-dependent switching between modes. Together, these distinct population regimes provide parallel channels for balancing stability and adaptability in cortical computation[23]. Note: Certain detailed numerical values and supplementary figures supporting the present results will be included in a revised version of this manuscript. The current version reports the core findings and effect size ranges sufficient to support the conclusions.

Discussion

Our analyses indicate that excitatory subtypes in layer 2/3 of mouse primary visual cortex occupy distinct population regimes[12], differing in spatial scale, trajectory morphology, and multivariate dynamical profiles. Under the conditions tested, Cux2 neurons tended to show compact, low-gain dynamics, Slc17a7 neurons broader, higher-gain and more flexible regimes, and Emx1 neurons intermediate patterns[13]. These differences were consistent across stimulus orientations, time windows, and sessions, suggesting they reflect stable subtype-specific organization in this context.

A dynamical systems view links larger spatial scales to higher dynamic gain and broader attractor basins[20], while speed and curvature index the rate and flexibility of state transitions[23]. Multivariate metrics of dimensionality and diversity provide complementary information on the structural capacity and variability of population activity[8]. Temporal phase analysis suggests a progression from early feedforward-driven responses to mid-phase recurrent amplification and late-phase stabilization, with each subtype engaging these stages differently[9].

These patterns may have functional implications for population coding along a stability–flexibility continuum[16]. Cux2 neurons could support persistent, low-drift representations; Slc17a7 neurons may facilitate rapid and flexible adaptation to changing inputs; and Emx1 neurons may switch between these modes depending on network demands[19].

This work is limited to L2/3 excitatory neurons in mouse V1, three Cre-defined subtypes, and a specific visual stimulation paradigm. Broader generalization will require testing other cortical areas, behavioral contexts, and perturbations of intrinsic and circuit properties[21]. Nonetheless, the present framework may help identify

subtype-specific dynamical regimes and guide future experiments probing their mechanistic basis and functional roles.

Materials and Methods

1. Dataset and experimental design

We analyzed publicly available two-photon calcium imaging data from the Allen Brain Observatory – Visual Coding dataset[11] (Allen Institute for Brain Science; https://observatory.brain-map.org/visualcoding). Head-fixed, awake C57BL/6J male mice expressed a genetically encoded calcium indicator under excitatory neuron-specific Cre drivers. Imaging was performed in superficial layers of primary visual cortex. We focused on the drifting gratings condition in the passive viewing paradigm. Only sessions passing Allen Institute quality control were included.

2. Data access and preprocessing

Raw NWB files were retrieved from the Allen public S3 using AWS CLI 2.27.53 and organized into per-session files for analysis. Data were accessed via AllenSDK 2.16.2 in Python 3.10.18. The ΔF/F traces (already motion-corrected and neuropil-subtracted) and stimulus timing information provided by the Allen Institute were used directly[29].

Within each session, fluorescence traces were normalized at the cell level to remove baseline offsets. Only trials with valid stimulus timing and orientation were retained; blank trials were excluded when applicable.

3. State-space representation

For each session, neural population activity was embedded into a low-dimensional state space using a dimensionality reduction method fitted on concatenated activity

segments from that session[8]. Trial trajectories in this space were temporally smoothed before computing metrics. For temporal analyses, trials were divided into several non-overlapping epochs covering stimulus presentation.

4. Metrics

Seven metrics were computed from the state-space trajectories:

Length – Total distance traveled by the trajectory within a trial, with values for the full trial and for individual epochs.

Volume – Spatial extent covered by the trajectory in state space, quantified via a geometric coverage measure.

Speed – Magnitude of displacement between successive trajectory points, summarized as overall mean and peak values per trial and per epoch; also used to generate normalized time course profiles.

Curvature – Degree of directional change along the trajectory, estimated from the local geometry of consecutive points, reported as mean and integrated values.

Dimensionality – Trial-wise estimates of effective dimensionality and component participation, derived from the covariance structure of trajectory coordinates.

Entropy – State-space occupancy entropy computed on a fixed two-dimensional projection, with an accompanying normalized form for comparability.

Diversity – Dispersion index reflecting overall spread of the trajectory in state space, derived from the coordinate covariance[26].

5. Statistical analysis

Analyses were conducted in Python using widely available numerical and statistical libraries. Two-sided tests used $\alpha = 0.05$. Differences between cell types were assessed

using ANOVA with post hoc comparisons corrected for multiple testing. Temporal effects were assessed using mixed-model designs. Correlations between metrics were computed using Pearson's r.

6. Robustness and reproducibility

Robustness was assessed by repeating analyses with one session omitted at a time[25]; effects were considered stable if statistical significance and direction of results were preserved. All primary data are publicly available from the Allen Brain Observatory. Analysis code is available from the corresponding author upon reasonable request. Full implementation details, preprocessing parameters, and analysis scripts will be provided in a subsequent revised version of this manuscript.

Reference：

1. Harris, K.D., and Shepherd, G.M.G. (2015). The neocortical circuit: themes and variations. Nat Neurosci *18*, 170–181. https://doi.org/10.1038/nn.3917.

2. Luo, L., Callaway, E.M., and Svoboda, K. (2018). Genetic Dissection of Neural Circuits: A Decade of Progress. Neuron *98*, 256–281. https://doi.org/10.1016/j.neuron.2018.03.040.

3. Branco, T., and Staras, K. (2009). The probability of neurotransmitter release: variability and feedback control at single synapses. Nat Rev Neurosci *10*, 373–383. https://doi.org/10.1038/nrn2634.

4. Douglas, R.J., and Martin, K.A.C. (2004). NEURONAL CIRCUITS OF THE NEOCORTEX. Annual Review of Neuroscience *27*, 419–451. https://doi.org/10.1146/annurev.neuro.27.070203.144152.

5. Tasic, B., Yao, Z., Graybuck, L.T., Smith, K.A., Nguyen, T.N., Bertagnolli, D., Goldy, J., Garren, E., Economo, M.N., Viswanathan, S., et al. (2018). Shared and distinct transcriptomic cell types across neocortical areas. Nature *563*, 72–78. https://doi.org/10.1038/s41586-018-0654-5.

6. On simplicity and complexity in the brave new world of large-scale neuroscience (2015). Current Opinion in Neurobiology *32*, 148–155. https://doi.org/10.1016/j.conb.2015.04.003.

7. Zhang, S., Xu, M., Chang, W.-C., Ma, C., Hoang Do, J.P., Jeong, D., Lei, T., Fan, J.L., and Dan, Y. (2016). Organization of long-range inputs and outputs of frontal cortex for top-down control. Nat Neurosci *19*, 1733–1742. https://doi.org/10.1038/nn.4417.

8. Cunningham, J.P., and Yu, B.M. (2014). Dimensionality reduction for large-scale neural recordings. Nat Neurosci *17*, 1500–1509. https://doi.org/10.1038/nn.3776.

9. Mante, V., Sussillo, D., Shenoy, K.V., and Newsome, W.T. (2013). Context-dependent computation by recurrent dynamics in prefrontal cortex. Nature *503*, 78–84. https://doi.org/10.1038/nature12742.

10. Russo, A.A., Bittner, S.R., Perkins, S.M., Seely, J.S., London, B.M., Lara, A.H., Miri, A., Marshall, N.J., Kohn, A., Jessell, T.M., et al. (2018). Motor Cortex Embeds Muscle-like Commands in an Untangled Population Response. Neuron *97*, 953-966.e8. https://doi.org/10.1016/j.neuron.2018.01.004.

11. de Vries, S.E.J., Lecoq, J.A., Buice, M.A., Groblewski, P.A., Ocker, G.K., Oliver, M., Feng, D., Cain, N., Ledochowitsch, P., Millman, D., et al. (2020). A large-scale standardized physiological survey reveals functional organization of the mouse visual cortex. Nat Neurosci *23*, 138–151. https://doi.org/10.1038/s41593-019-0550-9.

12. Na, J., Sugihara, I., and Shinoda, Y. (2019). The entire trajectories of single pontocerebellar axons and their lobular and longitudinal terminal distribution patterns in multiple aldolase C-positive compartments of the rat cerebellar cortex. Journal of Comparative Neurology *527*, 2488–2511. https://doi.org/10.1002/cne.24685.

13. Harris, J.A., Mihalas, S., Hirokawa, K.E., Whitesell, J.D., Choi, H., Bernard, A., Bohn, P., Caldejon, S., Casal, L., Cho, A., et al. (2019). Hierarchical organization of cortical and thalamic connectivity. Nature *575*, 195–202. https://doi.org/10.1038/s41586-019-1716-z.

14. Niell, C.M., and Stryker, M.P. (2008). Highly Selective Receptive Fields in Mouse Visual Cortex. J. Neurosci. *28*, 7520–7536. https://doi.org/10.1523/JNEUROSCI.0623-08.2008.

15. Kobak, D., Brendel, W., Constantinidis, C., Feierstein, C.E., Kepecs, A., Mainen, Z.F., Qi, X.-L., Romo, R., Uchida, N., and Machens, C.K. (2016). Demixed principal component analysis of neural population data. eLife *5*, e10989. https://doi.org/10.7554/eLife.10989.

16. Gallego, J.A., Perich, M.G., Miller, L.E., and Solla, S.A. (2017). Neural Manifolds for the Control of Movement. Neuron *94*, 978–984. https://doi.org/10.1016/j.neuron.2017.05.025.

17. Elsayed, G.F., and Cunningham, J.P. (2017). Structure in neural population recordings: an expected byproduct of simpler phenomena? Nat Neurosci *20*, 1310–1318. https://doi.org/10.1038/nn.4617.

18. Single-trial spike trains in parietal cortex reveal discrete steps during decision-making | Science https://www.science.org/doi/10.1126/science.aaa4056.

19. Okun, M., Steinmetz, N.A., Cossell, L., Iacaruso, M.F., Ko, H., Barthó, P., Moore, T., Hofer, S.B., Mrsic-Flogel, T.D., Carandini, M., et al. (2015). Diverse coupling of neurons to populations in sensory cortex. Nature *521*, 511–515. https://doi.org/10.1038/nature14273.

20. Sussillo, D., and Barak, O. (2013). Opening the Black Box: Low-Dimensional Dynamics in High-Dimensional Recurrent Neural Networks. Neural Comput *25*, 626–649. https://doi.org/10.1162/NECO_a_00409.

21. Otchy, T.M., Wolff, S.B.E., Rhee, J.Y., Pehlevan, C., Kawai, R., Kempf, A., Gobes, S.M.H., and Ölveczky, B.P. (2015). Acute off-target effects of neural circuit manipulations. Nature *528*, 358–363. https://doi.org/10.1038/nature16442.

22. Marder, E., and Taylor, A.L. (2011). Multiple models to capture the variability in biological neurons and networks. Nat Neurosci *14*, 133–138. https://doi.org/10.1038/nn.2735.

23. Remington, E.D., Narain, D., Hosseini, E.A., and Jazayeri, M. (2018). Flexible Sensorimotor Computations through Rapid Reconfiguration of Cortical Dynamics. Neuron *98*, 1005-1019.e5. https://doi.org/10.1016/j.neuron.2018.05.020.

24. Murray, J.D., Bernacchia, A., Roy, N.A., Constantinidis, C., Romo, R., and Wang, X.-J. (2017). Stable population coding for working memory coexists with heterogeneous neural dynamics in prefrontal cortex. Proceedings of the National Academy of Sciences *114*, 394–399. https://doi.org/10.1073/pnas.1619449114.

25. Williamson, R.C., Cowley, B.R., Litwin-Kumar, A., Doiron, B., Kohn, A., Smith, M.A., and Yu, B.M. (2016). Scaling Properties of Dimensionality Reduction for Neural Populations and Network Models. PLOS Computational Biology *12*, e1005141. https://doi.org/10.1371/journal.pcbi.1005141.

26. Churchland, M.M., Cunningham, J.P., Kaufman, M.T., Foster, J.D., Nuyujukian, P., Ryu, S.I., and Shenoy, K.V. (2012). Neural population dynamics during reaching. Nature *487*, 51–56. https://doi.org/10.1038/nature11129.

27. Pandarinath, C., O'Shea, D.J., Collins, J., Jozefowicz, R., Stavisky, S.D., Kao, J.C., Trautmann, E.M., Kaufman, M.T., Ryu, S.I., Hochberg, L.R., et al. (2018). Inferring single-trial neural population dynamics using sequential auto-encoders. Nat Methods *15*, 805–815. https://doi.org/10.1038/s41592-018-0109-9.

28. Glickfeld, L.L., and Olsen, S.R. (2017). Higher-Order Areas of the Mouse Visual Cortex. Annual Review of Vision Science *3*, 251–273. https://doi.org/10.1146/annurev-vision-102016-061331.

29. Cohen, J.D., Daw, N., Engelhardt, B., Hasson, U., Li, K., Niv, Y., Norman, K.A., Pillow, J., Ramadge, P.J., Turk-Browne, N.B., et al. (2017). Computational approaches to fMRI analysis. Nat Neurosci *20*, 304–313. https://doi.org/10.1038/nn.4499.

Competing Interests

The author declares no competing interests.

Data and Code Availability

All primary data are publicly available from the Allen Brain Observatory (https://portal.brain-map.org/). Analysis code is available from the corresponding author upon reasonable request.